Applied Catalysis B: Environmental 259 (2019) 118013

Contents lists available at ScienceDirect

Applied Catalysis B: Environmental

journal homepage: www.elsevier.com/locate/apcatb

Incorporating Mn cation as anchor to atomically disperse Pt on TiO_2 for low-temperature removal of formaldehyde

Jin Chen[a], Mingzhu Jiang[a,b], Wenjian Xu[a], Jing Chen[b,c,d], Zixiao Hong[a], Hongpeng Jia[a,b,*]

[a] CAS Center for Excellence in Regional Atmospheric Environment, and Key Laboratory of Urban Pollutant Conversion, Institute of Urban Environment, Chinese Academy of Sciences, Xiamen, 361021, China
[b] University of Chinese Academy of Sciences, Beijing, 100049, China
[c] Fujian Institute of Research on the Structure of Matter, Chinese Academy of Sciences, Fuzhou, Fujian 350002, China
[d] Xiamen Institute of Rare-earth Materials, Haixi Institutes, Chinese Academy of Sciences, Xiamen, Fujian 361021, China

ARTICLE INFO

Keywords:
Redox-driven hydrolysis
Platinum
Mn-TiO_2
Single atom
Catalytic oxidation

ABSTRACT

The redox-driven hydrolysis precipitation is developed to atomically disperse Pt on TiO_2 by involving high-valence Mn cations as the "anchor" into TiO_2. With multiple characterizations including Cs-HAADF-STEM and XAFS, single-atom state of Pt on the surface of support is evidenced. Due to high dispersion of Pt and strong interaction between Pt and MnO_x-TiO_2 (Mn-TiO_2), the physicochemical properties of catalysts are obviously improved. With combination of theoretical calculation and characterization, it is revealed that metallic Pt atom is stabilized by lattice oxygen of support. As observed, only 0.5% nominal amount of Pt loading (actual amount = 0.47%) on Mn-TiO_2 support can meet the demands of complete removal of HCHO with high/low concentrations and severe space velocity at low temperature. Through analysis of *in-situ* DRIFTS of HCHO, the catalytic oxidation of HCHO over Pt/Mn-TiO_2 obeys Mars-van-Krevelen mechanism. By associating with H-D exchange, it is found that introduction of water vapor can inhibit side-reactions and facilitate deep oxidation of HCHO.

1. Introduction

The development of single-atom catalysts has drawn more and more attention, because the high atom utilization significantly reduces the cost especially for catalysts containing noble metals [1]. Moreover, owing to low-coordination of atom environment and strong metal-support interaction, catalysts with atomic dispersion display remarkable activities in various reactions, *e.g.* electrocatalysis, oxidation, water-gas shift and hydrogenation [2–5]. For the achievement of atom dispersion, much effort has been made. For instance, Pt atomically dispersed in ferrum oxide (FeO_x) has been achieved by conventional co-precipitation and displayed turnover frequency as high as 13.6×10^2 s^{-1} for ambient temperature catalytic oxidation of CO [6]. However, a great amount of Pt atoms are lost in bulk of support, no longer serving as catalytic sites [3]. To further improve atom utilization, immobilization of active atoms on the surface of support is valid [1,3,7]. The functional groups (*e.g.* —NH_2, N heteroatom) or structural defects incorporated into the surface of support can stabilize single atom metal to avoid aggregation [1,3,8,9]. Nevertheless, this strategy suffers from easy loss of functional groups and high temperature for thermally inducing formation of surface defects. To overcome these problems, we have recently reported a novel method of redox-driven hydrolysis precipitation to support secondary metals such as Au and Ce on α-type manganese dioxide nanorod (OMS) with high dispersion even to atomic scale [10,11]. Within this method, the consumption of H^+ by redox reaction between H_2O_2 and OMS drives the deposit of alien cations on the chemically-etched surface [10,11]. However, this method is subjected to whether redox reaction between support and H_2O_2 occurs in an acidic medium, which is determined by redox potential of support (E^θ). For instance, H_2O_2 is incompetent to partial reduction of TiO_2, by considering higher E^θ value (0.695 V) for $O_2 + H^+ + 2e \leftrightharpoons H_2O_2$ than that (E^θ = —0.04 V) for $Ti^{4+} + e \leftrightharpoons Ti^{3+}$ [12].

Formaldehyde (HCHO) is considered as a noxious gaseous pollutant widely existing in indoor environment and industrial exhaust [27]. Among those applied technologies for removal of HCHO (*e.g.* adsorption, plasma, photo-degradation), catalytic oxidation is regarded as the most promising approach, owing to its easy handling and less secondary pollution [28–30]. For catalytic technology, the noble metal (*e.g.* Pt, Pd, Rh, Ir) catalysts usually exhibit higher activities than transition metal oxides in catalytic oxidation of HCHO at moderate condition as

* Corresponding author.
E-mail address: hpjia@iue.ac.cn (H. Jia).

https://doi.org/10.1016/j.apcatb.2019.118013
Received 6 June 2019; Received in revised form 19 July 2019; Accepted 27 July 2019
Available online 01 August 2019
0926-3373/

Table 1
A summary of recent reports about catalytic oxidation of HCHO over transition metal oxides and supported noble metal catalysts in flowing gas.

Catalyst	Preparation method	Reaction conditions	HCHO conversion/removal	Ref.
5Cu5Mn	Coprecipitation	1500 ppm, 20% O_2/N_2, 32,500 mL/(g h)	100%, 250 °C	[13]
Co_3O_4-rod	Precipitation	100 ppm, 21% O_2/N_2, 69,000 mL/(g h)	100%, 110 °C	[14]
3% Au/3DOM-CeO_2	Deposition–precipitation	0.06 vol% HCHO, 200 mg catalyst, Air, 66,000 mL/(g h)	100%, ~75 °C	[15]
3wt.% 3D-Au/Ce_3Co	Coprecipitation	50 ppm, Air, 20,000 mL/(h g),	100%, 60 °C	[16]
2K-8 wt.%Ag/Al_2O_3	Impregnation	110 ppm, 20% O_2/N_2, 100,000 mL/(g h), RH = 35%	100%, 65 °C	[17]
2.5% Ag/CeO2-P	Hydrothermal	810 ppm, 20% O_2/N_2, 84,000 /h	100% 110 °C	[18]
1.5 wt.% Rh/TiO_2	Impregnation	140 ppm, 20% O_2/N_2, 30,000 mL/(g h), RH = 50%	100%, 20 °C	[19]
Na-1%Ir/TiO_2	Precipitation-reduction	120 ppm, 20% O_2/N_2, 100,000 /h	100%, 25 °C	[20]
1% Pd/K-TiO_2	Impregnation-reduction	550 ppm, 20% O_2/N_2, 640,000 /h, RH = 30%	100%, 80 °C	[21]
1% Pd/TiO_2	Impregnation-reduction	140 ppm, 60 mg catalyst, 20% O_2/N_2, 95,000 /h	100%, 25 °C	[22]
2% Na-1% Pd/TiO_2	Impregnation-reduction	140 ppm, 60 mg catalyst, 20% O_2/N_2, 95,000 /h	100%, 25 °C	[23]
2% Na-1% Pt/TiO_2	Impregnation-reduction	600 ppm, 20% O_2/N_2, 120,000 /h	100%, 25 °C	[24]
1% Pt/TiO_2	Impregnation-reduction	26 ppm, 21% O_2/N_2, 60,000 /h	100%, 25 °C	[25]
0.5% Pt/$NaTiO_2$	Impregnation-reduction	650 ppm, 21% O_2/N_2,45000 mL/(g h), RH = 35%	100%, 40 °C	[26]

summarized by Table 1, where the support is commonly used to promote the stabilization and utilization of noble metals. According to literatures, the metallic species (Pt or Pd) within nanoparticles stabilized on TiO_2, as the key role for low-temperature catalytic oxidation, can proceed the HCHO removal at room temperature and even freezing temperature [22,24,25,31]. However, there are still some scientific problems with respect to reaction mechanism and water effect to be clear. Furthermore, it is promising to further reduce the cost of catalyst by improving atomic utilization of noble metal, which is meaningful to widely expanding application of environmental catalysis, since percentage amount of noble metals is still demanded by most of catalysts for absolute removal of HCHO at high space velocity.

In this work, we have attempted to functionalize TiO_2 by incorporating high-valence Mn cations as the "anchor" of atomic noble metal. The high-valence species of Mn^{4+} and Mn^{3+} ions is reduced by H_2O_2 in acidic medium as follows: $MnO_2 + H_2O_2 + 2H^+ = Mn^{2+} + 2H_2O + O_2$ (ΔG^θ = —102.1 kJ/mol) and $Mn_2O_3 + 4H^+ + H_2O_2 = 2Mn^{2+} + 3H_2O + O_2$ (ΔG^θ = —152.5 kJ/mol) [10,12]. For consumption of H^+ by redox reaction, the hydrolysis of H_2PtCl_6 into Pt $(OH)_4$ colloids is driven to release more H^+ as follows: $H_2PtCl_6 + 3H_2O = Pt(OH)_4 + 4HCl$. Meanwhile, the charge balance of support is broken, due to the reduction of Mn^{4+} and Mn^{3+} to soluble Mn^{2+} cations, so the negatively charged surface is apt to adsorb Pt^{4+} ions. Therefore, Pt ions are loaded firmly on the surface of Mn-TiO_2 by redox-driven hydrolysis precipitation. By inspecting Cs-HAADF-STEM and XAFS of the catalyst, the feasibility of this strategy to atomically disperse Pt on Ti-based oxides is evidenced. The as-prepared Pt catalysts are applied in catalytic oxidation of formaldehyde (HCHO) at ambient temperature or below. Through correlation between characterizations and catalytic performance, the coordination environment of Pt atom, reaction mechanism and water effect are revealed.

2. Experimental section

2.1. Chemicals and materials

Potassium permanganate ($KMnO_4$), hydrogen peroxide (H_2O_2, 30 wt.%) and polyformaldehyde with purity of A.R. grade were all purchased from Sinopharm Chemical Reagent Co., Ltd. (Shanghai, China). Titanium sulfate ($TiOSO_4$, 98 wt.%) was bought from Xiya Reagent Co., Ltd. (Shandong, China). Chloroplatinic acid ($H_2PtCl_6{\cdot}6H_2O$, 38 wt.% content of Pt) was bought from Kaida Chemical Engineering Co., Ltd. (Shaanxi, China).

2.2. Materials preparation

Mn-doped TiO_2 (Mn-TiO_2) as the support was prepared by hydrothermal reaction. The procedures are described in detail as follows: 10 g of $TiOSO_4$ and 0.5 g of $KMnO_4$ were dissolved in 500 mL deionized water under vigorous stirring, and the resulting solution was transferred to autoclave and heated at 160 °C for 24 h. The obtained greenish solid was filtered and washed with water, and finally the powder was calcined at 450 °C for 4 h. Pure TiO_2 as a control sample was synthesized through the same procedures without addition of $KMnO_4$. The procedures of supporting Pt on Mn-TiO_2 *via* redox-driven hydrolysis precipitation are similar to our previous work [10], but the reaction temperature is controlled at 60 °C due to high-valence Mn cations strongly trapped by the skeleton of TiO_2. As an example, the sample of nominal 0.5% Pt loading was prepared as follows: 2 g of Mn-TiO_2 was ultrasonically dispersed in 100 mL of aqueous solution containing 0.051 mmol of H_2PtCl_6 to obtain the suspension solution. 0.5 g of H_2O_2 (30 wt.%) was diluted by 20 mL of water and then was dropwise added to the above suspension under vigorous stirring at 60 °C. The resulting solids were filtered, washed with water and dried at 110 °C overnight. Finally, the obtained powder was treated by pure H_2 at 350 °C for 4 h. According to the nominal content of Pt, these catalysts were denoted as *x*% Pt/Mn-TiO_2. As a control sample, H_2-Mn-TiO_2 was prepared by H_2 reduction of Mn-TiO_2 at 350 °C.

2.3. Materials characterization

Powder X-ray diffraction (XRD) measurements were performed on PANalytical X'pert Pro instrument equipped with X-ray source of Cu-Kα. The scanning range of 2θ angle was from 10° to 90°. Transmission electronic microscopy (TEM) and high angle angular dark field scanning transmission electron microscope (HAADF-STEM) were taken by JEM 2100 F electronic microscopy. Spherical aberration corrected HAADF-STEM (Cs-HAADF-STEM) was taken on JEM ARM 200 F. The elemental distribution was visualized by energy dispersive spectroscopy (EDS) of Oxford Instruments. X-ray absorption fine structure (XAFS) of Pt-L_3 edge was measured in transmission mode at room temperature on the BL14W1beam line of Shanghai Synchrotron Radiation Facility (Shanghai City, China). X-ray photoelectron spectroscopy (XPS) of Thermo Scientific ESCALAB 250 instrument and Shimadzu Kratos Supra Axis instrument were used. The metal element contents were detected by using inductively coupled plasma-optical emission spectroscopy (ICP-OES). N_2 static physisorption characterization was performed on Quantachrome Autosorb IQ instrument. The specific surface area (S_{BET}) and pore size (D_{BJH}) were calculated by means of Brunauer-Emmett-Teller (BET) and Barrett-Joyner-Halenda (BJH) methods. H_2 temperature-programed reduction (H_2-TPR) and temperature-programed desorption (such as CO-TPD, O_2-TPD and HCHO-TPD) were performed on ChemStar TPx chemisorption analyzer of Quantachrome. *In-situ* diffuse reflectance Fourier transform infrared spectroscopy (*in-situ* DRIFTS) was carried out on Thermo Fisher is50 instrument equipped with Harrick *in-situ* cell. Among them, the procedures for characterizations of

H_2-TPR, CO-TPD, O_2-TPD, HCHO-TPD and *in-situ* DRIFTS were described in detail in Appendix A. Supplementary data.

2.4. Activity test

The catalytic performances in removing HCHO of high concentration (100 ppm) and low concentration (about 8 ppm) were both examined. For the removal of high-concentration HCHO, the activity was tested in U-type tube (i.d. = 5.0 mm) and the temperature was controlled by cooling tank. Before evaluation, the catalyst and silica sand were screened by using sieves of 40–60 mesh. About 66 mg of catalyst and 2 g of silica sand were mixed to keep the length of reaction layer at about 3 cm. The feed gas was generated by passing pure air through polyformaldehyde and water saturator. The powder of polyformaldehyde was pretreated by heating at 60 °C for 24 h to remove easily volatile compounds. By controlling flow rate and temperature of saturator, weight hourly space velocity (WHSV) and relative humidity (RH) were adjusted. For example, the reaction conditions of WHSV = 60,000 mL/(g h), RH = 50% and 100 ppm HCHO were conducted by passing a pure air stream with the flow rate of 33.3 mL/min through polyformaldehyde at 33 °C and another air stream with the flow rate of 33.3 mL/min through water at 25 °C. It should be noted the amount and granulometric fraction of catalysts and the total gaseous stream were selected to be in a true kinetic regime, *i.e.* beyond the internal and external diffusion limits [32]. According to the difference of CO_2 concentration in effluent stream monitored by gas chromatography, CO_2 yield from oxidation of HCHO was calculated as following: CO_2 yield = $c(CO_2)/c_{complete}(CO_2)$ × 100%. It should be noted that $c_{complete}(CO_2)$ is CO_2 concentration when HCHO is completely oxidized into CO_2. A mineralization tube was designed by filling 1% Pd/CeO_2 catalyst and run at 200 °C for complete oxidation of inlet HCHO into CO_2, thus the initial concentration of HCHO was gained by measuring CO_2 concentration. The instrument picture was shown in Appendix A. Supplementary data. For the removal of low-concentration HCHO, the performance was evaluated at room temperature with conditions of WHSV = 120,000 mL/(g h) and RH = 50%. The residual HCHO in fluent gas was detected manually by using Formaldemeter™ *htV-M* instrument.

3. Results and discussion

3.1. Structural analysis

As mentioned above, the support is the key to determine the feasibility of this strategy. As characterized by XRD in Fig. 1(a), Mn-TiO_2 exhibits a classic anatase structure (PDF # 00-021-1272), but the characteristic peaks especially at about 25.3° (2θ) are obviously shifted to lower angle compared to pure TiO_2, as the symbol of doping Mn ions into lattice. The composition of catalysts detected by ICP-OES (in Table 2) demonstrates the actual amount of Pt loading is close to nominal value, but Mn content decreases slightly after introducing Pt, which is ascribed to leaching of Mn cations during redox-driven hydrolysis. N_2 static physisorption in Fig. 1(b) shows similar V-type isotherm for all as-prepared materials and major pore diameter maximized at 6.7 nm. With analytic methods of Brunauer-Emmett-Teller (BET) and Barrett-Joyner-Halenda (BJH), the specific surface area (S_{BET}) and mean diameter (D_{BJH}) are calculated. In Table 2, the higher values of S_{BET} and D_{BJH} for *x*% Pt/Mn-TiO_2 than those for Mn-TiO_2 are attributed to some loss of Mn by chemical etching. Generally, the more defects derived from chemical etching, the more exposure of active sites that can facilitate catalytic reaction.

The 0.5% Pt/Mn-TiO_2 was selected as an example of as-prepared materials. As observed for TEM and HAADF-STEM in Fig. 2(a–b), none of Pt nanoparticles are detected. However, homogeneous distribution of Pt at the same district of HAADF-STEM is visualized by EDS mapping in Fig. 2(c), implying Pt exists in the state of ultra-small size. With

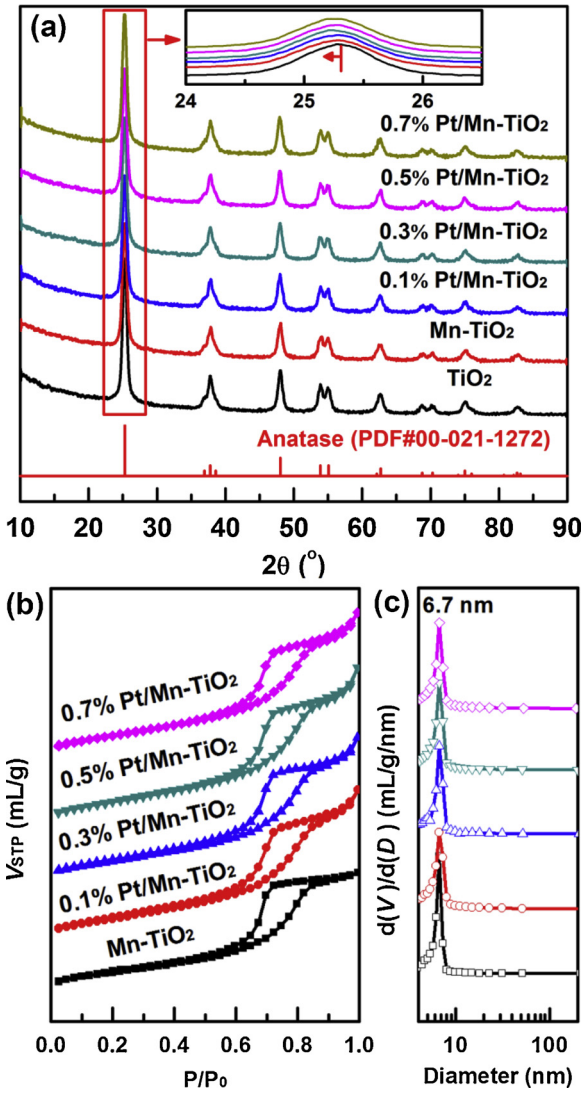

Fig. 1. Structural characterization of the samples. (a) XRD patterns, (b) isotherm curves of N_2 static adsorption-desorption, and (c) diameter distribution of pore-channel.

Table 2
Physical properties and apparent activation energy (E_{App}) for HCHO catalytic oxidation of various samples.

Sample	Element content (wt.%)		D_{BJH} (nm)	S_{BET} (m^2/g)	O_{Latt}/O_{Ads}	E_{App} (kJ/mol)
	Pt	Mn				
Mn-TiO_2	/	3.63	8.2	80.5	4.39	/
0.10% Pt/Mn-TiO_2	0.08	3.32	8.8	95.2	5.19	58.92
0.30% Pt/Mn-TiO_2	0.34	3.43	8.7	92.2	5.18	60.12
0.50% Pt/Mn-TiO_2	0.47	3.26	9.2	94.1	5.14	58.97
0.70% Pt/Mn-TiO_2	0.64	3.34	9.0	92.1	5.14	57.05

spherical aberration corrected HAADF-STEM (Cs-HAADF-STEM) in Fig. 2(d), a lot of bright dots appearing lonely at intervals between {101} planes of TiO_2 are assigned to Pt atoms. More evidences for single atom are given by XAFS. By k^3-weighted Fourier transforming normalized Pt-L_3 edge of XAFS spectra in Fig. 2(e), the radius (R) of

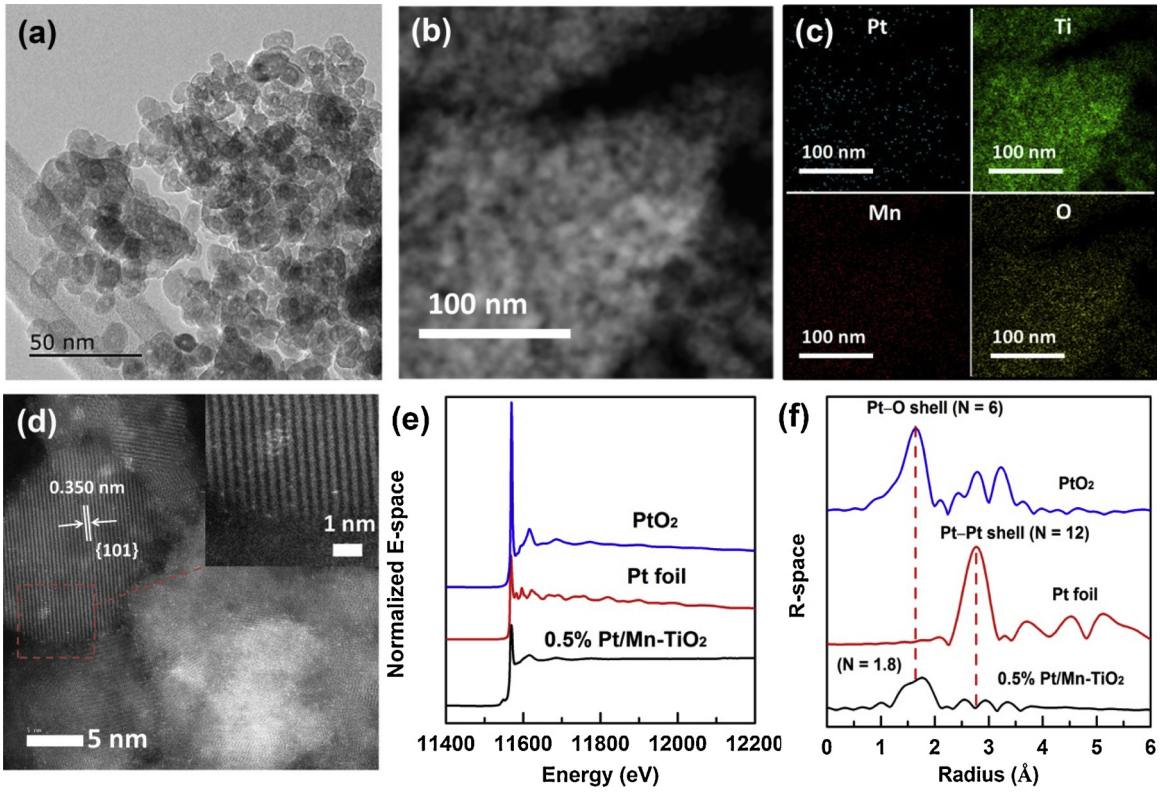

Fig. 2. (a–d) TEM, HAADF-STEM, EDS mapping and Cs-HAADF-STEM images of 0.5% Pt/Mn-TiO_2, respectively, (e) normalized Pt-L_3 edge of XAFS spectra, (f) k^3-weighted Fourier transformed XAFS.

coordination shell for Pt atom is calculated [33]. As displayed in Fig. 2(f), the coordination radius of Pt atoms is obviously closer to Pt—O bond of PtO_2 standard sample and is shorter than Pt—Pt bond of Pt foil, which confirms the existence of single-atom Pt. Moreover, the coordination number (N) of Pt—O for 0.5% Pt/Mn-TiO_2 is only 1.8, which means highly-unsaturated coordination of Pt. In one word, all the evidence points to the success of redox-driven hydrolysis precipitation in supporting single-atom Pt on Mn-TiO_2.

Single-atom Pt of highly-unsaturated coordination has strong chemical adsorption of CO, so the temperature of CO desorption increases from 344 °C for Mn-TiO_2 to 440 °C for 0.5% Pt/Mn-TiO_2 as depicted in Fig. 3. Mn cations with the lack of *d*-orbital electrons chemically adsorb CO and some physical adsorption of CO is also observed, resulting in appearance of two peaks at 2114 cm^{-1} and 2173 cm^{-1} for *in-situ* CO-DRIFTS of Mn-TiO_2 in Fig. 4, respectively [34]. CO is mainly linearly

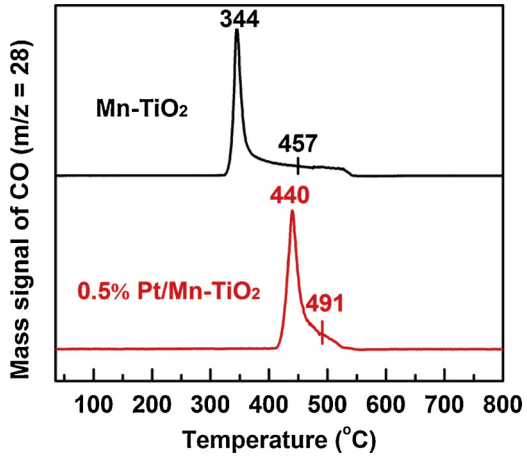

Fig. 3. CO-TPD of Mn-TiO_2 and 0.5% Pt/Mn-TiO_2.

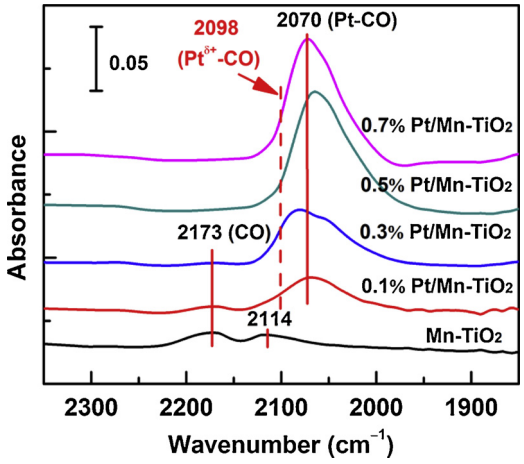

Fig. 4. *In-situ* CO-DRIFTS of Mn-TiO_2 and supported Pt catalysts.

adsorbed by Pt, causing a peak maximized at 2070 cm^{-1} for *in-situ* CO-DRIFTS of *x*% Pt/Mn-TiO_2. In fact, the peak for bridge-type adsorption of CO (Pt—CO—Pt) at around 2000 cm^{-1} is absent due to single-atom dispersion of Pt. Compared to the peak at 2098 cm^{-1} for linear adsorption of CO by ionic Pt (Ptδ^+—CO) [3], the lower wavenumber of Pt—CO bond (*ca.* 2070 cm^{-1}) for *x*% Pt/Mn-TiO_2 indicates that the Pt species are mainly existed as the metallic state.

Given high sensitivity of XPS to valence change of surficial species, the valence state of Pt is further inspected. As shown in Fig. 5(a), the majority of Pt atoms stay at metallic state which is in accordance with the observation from *in-situ* CO-DRIFTS. Metallic Pt acting as active site is retained by the TiO_2 support, due to electron donation of Ti^{3+} cations [24,25]. With comparison of Ti-2p profiles in Fig. 5(b), the characteristic peaks are shifted to low binding energy (B.E.) after Pt loading, as a symbol for formation of more Ti^{3+} cations [35]. Nevertheless, Ti-2p

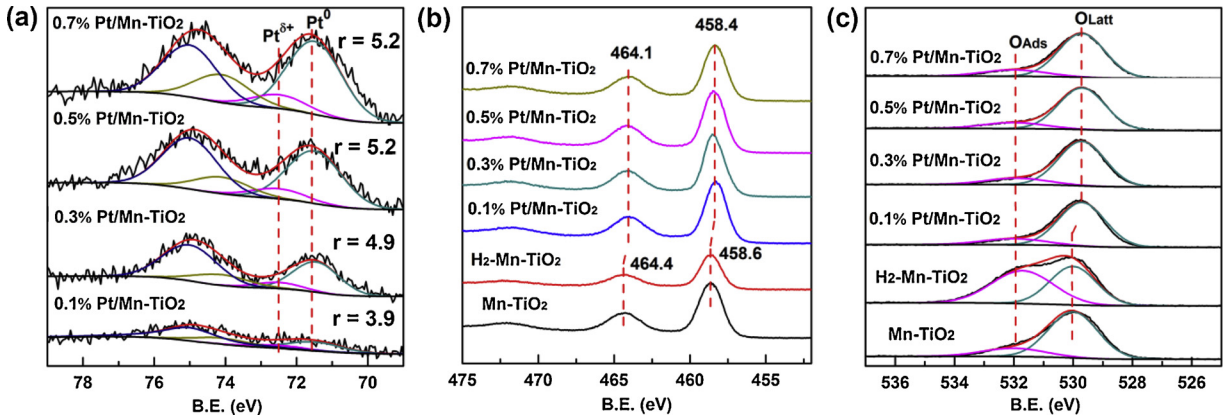

Fig. 5. XPS profiles of (a) Pd-4f orbital with peak ratios of Pt^0 and $Pt\delta^+$ (r = $Pt^0/Pt\delta^+$), (b) Ti-2p orbital, and (c) O-1 s orbital.

spectrum of H_2-Mn-TiO_2 as a control sample is similar to Mn-TiO_2, implying no change to valence of Ti species through H_2 reduction in absence of Pt. It also indicates that Pt addition has a strong interaction to Mn-TiO_2. Because of strong metal-support interaction (SMSI) effect, the electrons of Ti^{3+} cations are partially transferred to Pt, so low-valence Ti cations are stabilized and metallic Pt is retained [36]. The similar valence changes happen to Mn species, as shown in Fig. S2. As a result, more proportion of Mn^{3+} and Mn^{4+} cations are transformed to Mn^{2+} in presence of Pt by comparison of results.

With valence change of metal ions, the oxygen species is also influenced. As depicted in Fig. 5(c), the O-1 s peaks of Mn-TiO_2 at 530.0 eV and 531.9 eV are assigned to lattice oxygen (O_{Latt}) and adsorbed oxygen (O_{Ads}), respectively [22]. Herein, O_{Ads} includes surficial hydroxyl and physically-adsorbed oxygen species. Compared to pure Mn-TiO_2, the introduction of Pt leads to the shift of O_{Latt} peak from 530.0 eV to 529.7 eV, but the position of O_{Ads} is not changed. It is proposed that Pt directly interacts with O_{Latt} of Mn-TiO_2. The strong interaction facilitates the mobility of O_{Latt} from bulk to surface, so *x*% Pt/Mn-TiO_2 has O_{Latt}/O_{Ads} ratio of around 5.14 which is higher than that of Mn-TiO_2 (4.39) (in Table 2). On the contrary, the O_{Latt} content of H_2-Mn-TiO_2 decreases, which is possibly ascribed to easy loss of unstable O_{Latt} and replacement by molecular/water oxygen in absence of Pt with exposure to aerobic atmosphere.

The acceleration of oxygen mobility driven by SMSI effect is also reflected on O_2-TPD. As shown in Fig. 6, there are multiple peaks at the spectrum of pure Mn-TiO_2. According to temperature, the peaks maximized at 144 °C, 238 °C, 483 °C and 726 °C are assigned to desorption of chemically adsorbed O_{Ads}, surficial O_{Latt}, O_{Latt} in bulk, and oxygen species from deep decomposition of metal oxide, respectively [37]. The

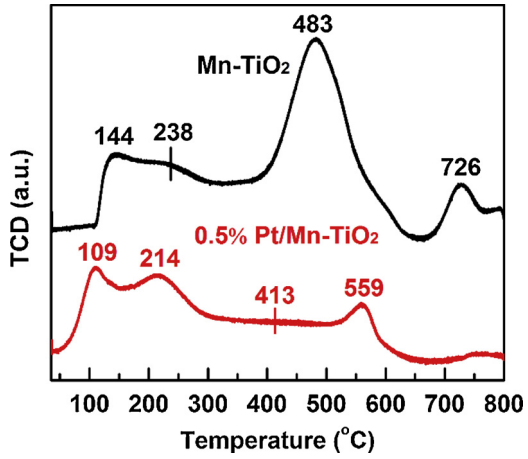

Fig. 6. O_2-TPD of Mn-TiO_2 and 0.5% Pt/Mn-TiO_2.

corresponding four peaks also appear at O_2-TPD of 0.5% Pt/Mn-TiO_2, but the temperatures decrease obviously. Meanwhile, the peak for desorption of surficial O_{Latt} at 214 °C becomes larger and the peak at 413 °C belonging to O_{Latt} in bulk becomes smaller, which confirms the migration of lattice oxygen from deep layer to surface. In conclusion, the introduction of Pt facilitates mobility of oxygen species within metal oxide support, which can accelerate oxygen cycle during catalytic oxidation reaction.

With the help of density function theory (DFT), more information about the strong interaction between Pt and support is obtained, and concurrently it is proved that some donation of electron from support to Pt results in the formation of electron-rich Pt and electron-deficient O_{Latt}. Based on image of Cs-HAADF-STEM, Pt atoms are mainly laid on {101} lattice plane of TiO_2. Moreover, {101} lattice plane as the most stable one among various planes of TiO_2 has been studied by many researchers [38–40]. According to structural characteristics of TiO_2 {101} planes [38], a cluster of $H_2Ti_2O_2(OH)_2$ is built in MaterialStudio software with an aim to recognize the possible coordination site between Pt and the support. Allowing for a little content and chemically leaching of Mn cations within support during preparation, Mn atoms are neglected for simplification of analytic model. For proposed cluster, the connected oxygen atoms in Ti—O—Ti and Ti—OH are O_{Latt} and hydroxyl oxygen, respectively. Several possible types of coordination between Pt and O atoms are constructed as drawn in Table S1. The DFT calculations using the exchange-correlation functional of GGA-PW91 approximation are performed with the program package $DMol^3$. With $Dmol^3$ program and the similar setting parameters to the literature [38], the minimized formation energies (E_f) for different types are calculated *via* geometry optimization, so relative energies of molecule stabilization are obtained as described in Fig. 7. Because of its lowest energy, the type IV structure is the most stable, suggesting that the strong interaction mainly occurs between Pt and O_{Latt} atoms. This result is consistent with XPS as mentioned above, and is similar to the published work where Pd atom coordinated with O_{Latt} (remarked as O_{2c} in the literature) on (101) plane of TiO_2 is the most stable, though Cambridge Sequential Total Energy Package (CASTEP) is instead of $Dmol^3$ [39]. Meanwhile, the distribution of Fukui electrons upon each atom of type IV structure is calculated by Mulliken and Hirshfeld functions. The electron distribution differs with reaction types, so the relative electron densities at models of Fukui (—), Fukui (+) and Fukui (0) (for nucleophile, electrophile and radical reactions, respectively) are computed. As shown in Table 3, the electron density of O_{Latt} interconnected with Pt atom, namely numbered as O(4), is lower than that of another unconnected O_{Latt} in any case. Companying with the decreased electron density of O(4), more electrons are accumulated on coordinated Pt atom. These results demonstrate TiO_2-based support donates electron to Pt *via* interaction between Pt and surficial O_{Latt} species. In fact, electron-rich Pt can activate molecular oxygen by donation of extra

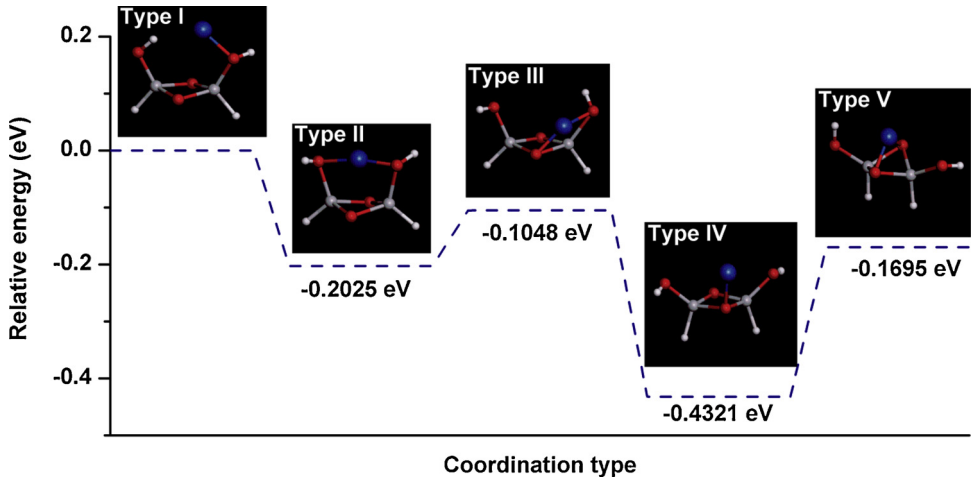

Fig. 7. Relative energies of different coordination types.

electron, and electron-deficient O_{Latt} is apt to attracting electron from reductive molecule like HCHO.

Because of electron transfer as mentioned above, the reducibility is modified by supporting Pt, which is reflected on H_2-TPR. As displayed in Fig. 8, a broad peak at 497 °C belongs to reduction of Mn^{4+} and Mn^{3+} into Mn^{2+}, and a sharp peak at 567 °C is attributed to reduction of Ti^{4+} to Ti^{3+} on surface of Mn-TiO_2. With dispersing Pt on Mn-TiO_2, several obvious changes take place to 0.5% Pt/Mn-TiO_2. A slight peak appears at 98 °C is due to the consumption of H_2 by physically adsorbed oxygen and a unsymmetrical peak at about 377 °C are ascribed to the reduction of high-valence Mn cations (Mn^{4+} and Mn^{3+}) and surficial Ti^{4+} species. Meanwhile, a broad peak located at 555 °C corresponds to H_2 consumption by reductive species in bulk. Obviously, the reduction temperatures are reduced with Pt loading, which means the improvement of reducibility. Generally, physicochemical properties in terms of reducibility, oxygen mobility and charged state are the decisive factors to catalytic performance.

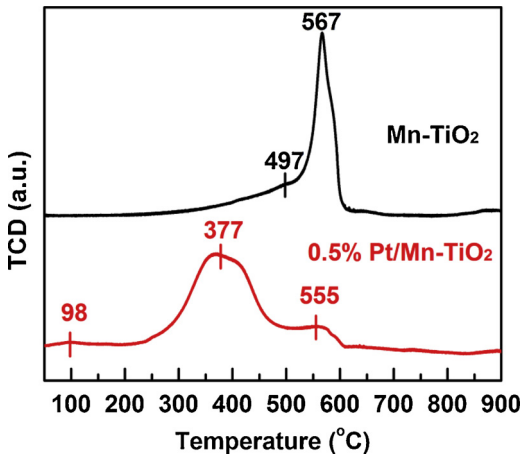

Fig. 8. H_2-TPR of Mn-TiO_2 and 0.5% Pt/Mn-TiO_2.

3.2. Catalytic performance in oxidation of HCHO

The activities in catalyzing oxidation of high-concentration HCHO (100 ppm) are evaluated under conditions of WHSV = 60,000 mL/(g h) and RH = 50%. As shown in Fig. 9(a), the temperature-dependent CO_2 yield is facilitated after Pt loading and is promoted with the increasing of Pt content. For clear comparison, CO_2 yield at each temperature is averaged and plotted as Fig. 9(b). The similar activities are performed by 0.5% Pt/Mn-TiO_2 and 0.7% Pt/Mn-TiO_2 under this condition. Complete oxidation of HCHO into CO_2 is achieved at above 15 °C, and CO_2 yield can reach to 20% even at freezing temperature over *x*% Pt/Mn-TiO_2 (x = 0.5 and 0.7). Considering the more Pt content and the higher cost, 0.5% Pt/Mn-TiO_2 is screened out as an optimal catalyst with high activity and relatively-low cost. Furthermore, over catalysts with low Pt loading (0.1% and 0.3%), an abnormal phenomenon can be observed that the elevated reaction temperature is not able to further improve CO_2 yield and conversely inhibits mineralization of HCHO. The similar phenomenon has ever observed for catalytic CO oxidation due to competitive adsorption on the surface of catalyst [41,42]. After XPS analysis for treated catalyst (Fig. S3), it displays the enhanced signal of charged Pt species, indicating more charged Pt formed in the reaction process. The treated 0.5% Pt/Mn-TiO_2 has higher value of Pt^0/

Table 3
The Fukui electron distribution for type IV.

	Atom	Fukui (-)		Fukui (+)		Fukui (0)	
		Mulliken	Hirshfeld	Mulliken	Hirshfeld	Mulliken	Hirshfeld
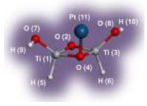	Ti (1)	0.017	0.089	0.073	0.166	0.045	0.127
	O (2)	0.056	0.044	0.057	0.064	0.056	0.054
	Ti (3)	0.013	0.088	0.065	0.16	0.039	0.124
	O (4)	0.014	0.032	0.048	0.045	0.031	0.038
	H (5)	0.142	0.077	0.161	0.089	0.152	0.083
	H (6)	0.143	0.077	0.16	0.09	0.152	0.083
	O (7)	0.043	0.049	0.07	0.063	0.057	0.056
	O (8)	0.041	0.051	0.068	0.06	0.054	0.056
	H (9)	0.032	0.028	0.041	0.037	0.037	0.033
	H (10)	0.035	0.029	0.04	0.035	0.037	0.032
	Pt (11)	0.463	0.437	0.217	0.19	0.34	0.314

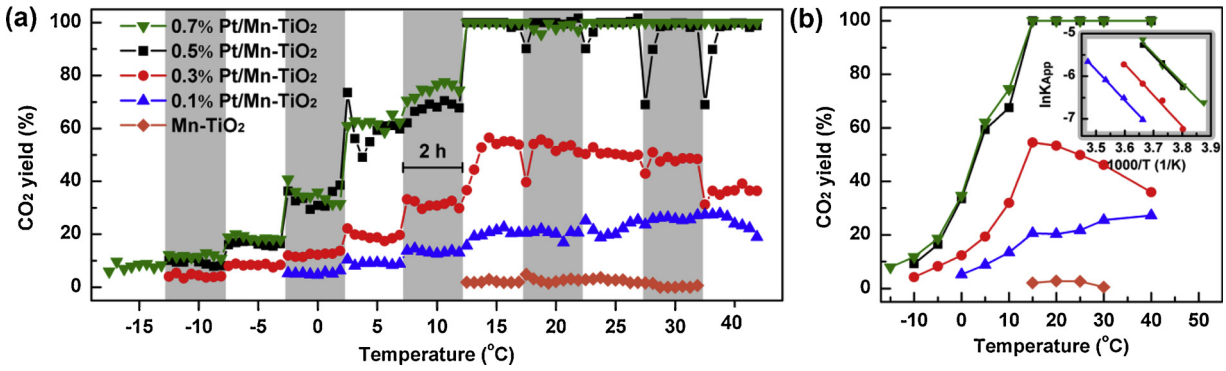

Fig. 9. (a) The catalytic performance in oxidation of high-concentration HCHO (about 100 ppm, WHSV =60,000 mL/(g h)) at RH = 50%, (b) average temperature-dependent CO_2 yield from oxidation of high-concentration HCHO and Arrhenius plots (inset).

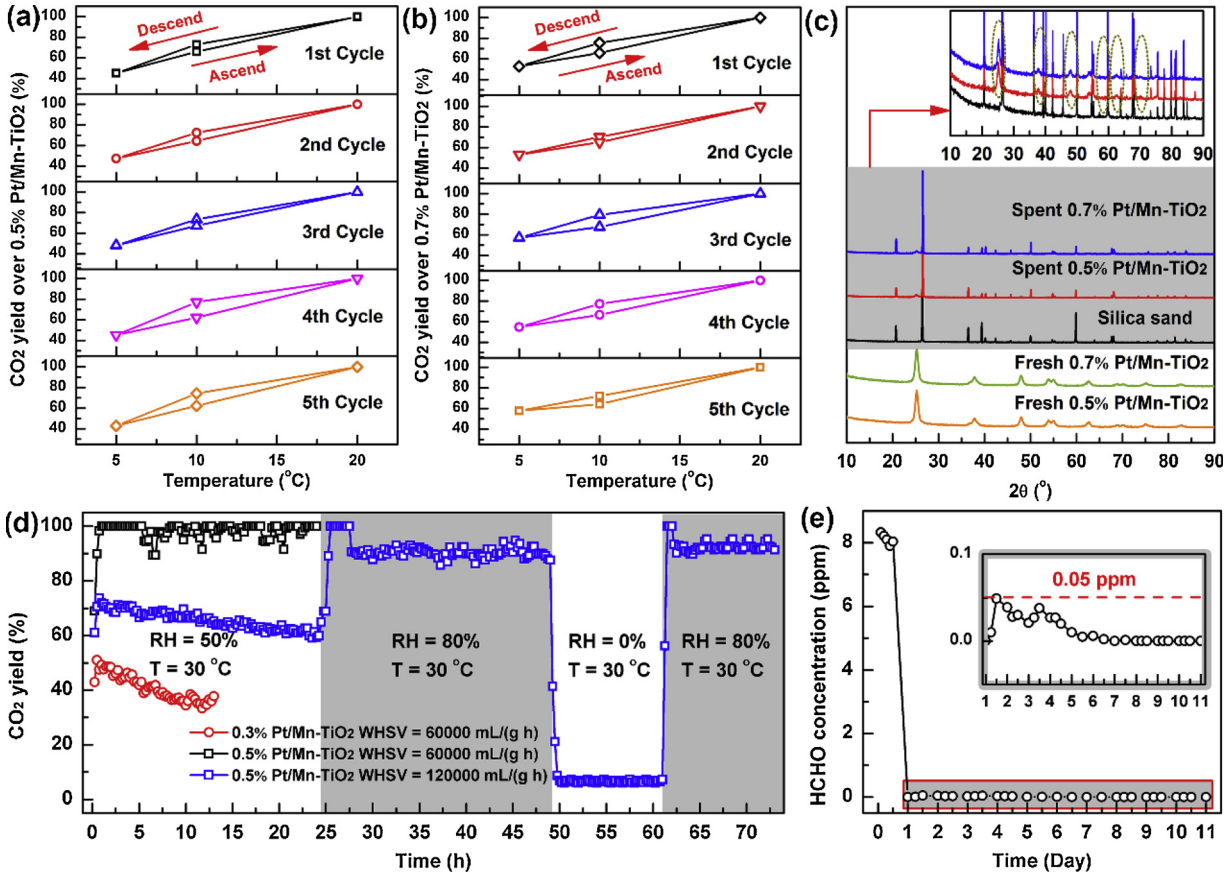

Fig. 10. (a–b) Descend/ascend cycle of activity test on 0.5% Pt/Mn-TiO_2 and 0.7% Pt/Mn-TiO_2 in catalytic oxidation of HCHO into CO_2 (WHSV = 60,000 mL/(g h), RH = 50%), (c) XRD patterns of spent catalysts after 5 cycles and the enlarged profile (insert), (d) stability test for high-concentration HCHO with different RH and WHSV, (e) stability test for removal of low-concentration HCHO (about 8 ppm, WHSV = 120,000 mL/(g h)) at room temperature and RH = 50%.

$Pt^+\delta$ ratio (3.3) than that of treated 0.3% Pt/Mn-TiO_2 ($Pt^0/Pt^+\delta$ = 2.3) as depicted in Fig. S3. Compared to fresh catalysts, the treated 0.5% Pt/Mn-TiO_2 has less reduction of $Pt^0/Pt^+\delta$ ratio than the treated 0.3% Pt/Mn-TiO_2, exhibiting better oxidation resistance at high temperature. Therefore, it explains that the catalytic efficiency of catalysts with above 0.5% Pt loading is remained even when reaction temperature reaches to 40 °C, because the metallic Pt serves as the main active site [22,24,25,31].

By dynamic study, the apparent activation energy (E_{App}) values for catalytic oxidation of HCHO are calculated. All the E_{App} values are close to 60 kJ/mol as listed in Table 2, though catalysts contain different contents of Pt. When CO_2 yield is less than 20% for dynamic study, the reaction process obeys kinetic control, so the reaction rate is determined by the amount and reactivity of active sites. As evidenced by characterization, the catalytically-active Pt atoms are all isolated and dispersed on the surface of Mn-TiO_2, so reaction rate of HCHO oxidation is positively related to the amount of Pt loading. Generally, the constant barrier energy is overcome by the same active site. In other words, the close values of E_{App} implies that the active sites within catalysts containing different Pt content are similar.

The recyclability of 0.5% Pt/Mn-TiO_2 and 0.7% Pt/Mn-TiO_2 is evaluated by descend/ascend cycle of activity test. As depicted in Fig. 10(a–b), after five cycles, both of 0.5% and 0.7% Pt/Mn-TiO_2 exhibit the good recyclability of catalytic performance. The XRD results in Fig. 10(c) demonstrate none of obvious change takes place to the structure of spent catalysts after 5 cycles. It should be pointed out that

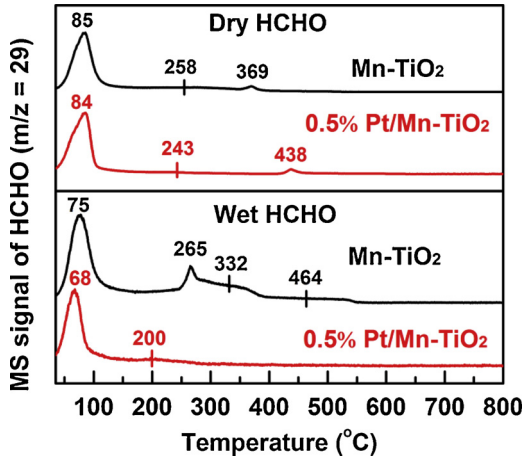

Fig. 11. HCHO-TPD of Mn-TiO_2 and 0.5% Pt/Mn-TiO_2 at dry and wet conditions.

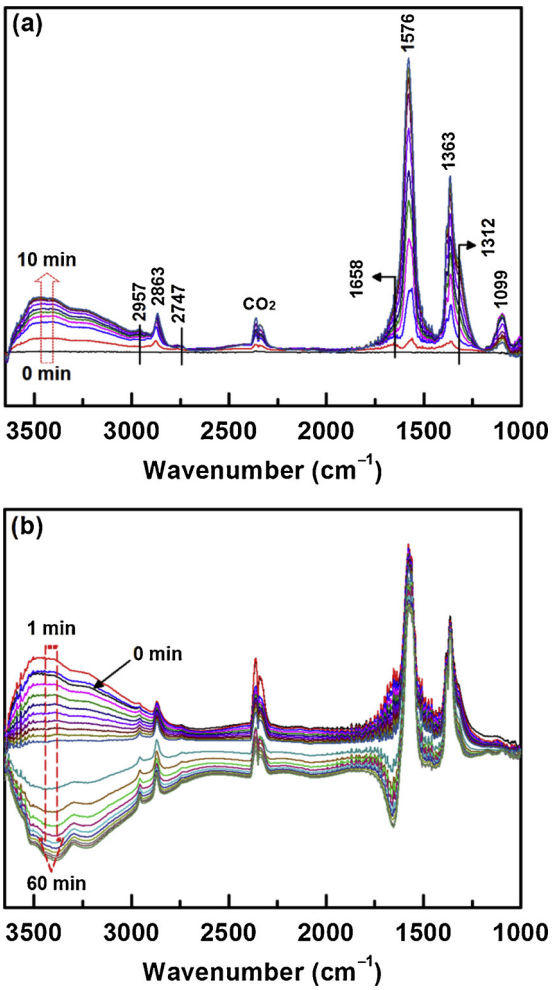

Fig. 12. *In-situ* DRIFTS of HCHO oxidation over 0.5% Pt/Mn-TiO_2, (a) adsorption of HCHO, (b) 20% O_2/He flowing through sample layer at room temperature.

some sharp diffraction peaks belong to silica sand that is used to disperse catalyst for adjusting the length of reaction layer. The characteristic peaks of catalysts are weaker compared to that of silica sand as depicted in insert of Fig. 10(c). During long-term activity test as shown in Fig. 10(d), 0.5% Pt/Mn-TiO_2 displays higher activity than 0.3% Pt/Mn-TiO_2 and remarkable long-term stability even at WHSV as high as 120,000 mL/(g h). It is also found high RH is favorable to catalytic oxidation. Hence, more than 90% CO_2 yield is reached in the case of RH = 80%, but CO_2 yield decreases dramatically to below 10% when dry air is used. The similar changes occur to the stability test of 0.7% Pt/Mn-TiO_2 when WHSV is increased and feed gas is replaced by dry air, as depicted in Fig. S4. By considering low concentration of indoor HCHO, the performance in removal of low-concentration HCHO (about 8 ppm) is examined. At ambient condition, the concentration of HCHO is fast reduced to less than 0.05 ppm arriving at current indoor air quality standards of China [43]. During continuous test time of 11 days, the activity almost keeps a constant as depicted in Fig. 10(e).

In fact, the performance of as-prepared catalyst in oxidation of HCHO is closely related to participation of water vapor as seen in activity test, which is also observed by Li et al. [22]. To reveal the inner principle, HCHO-TPD is applied. As depicted by Fig. 11, three desorption peaks occur to Mn-TiO_2 at dry condition. The one maximized at 85 °C is ascribed to physically adsorbed HCHO, but it is difficult to recognize the two broad peaks at 258 °C and 369 °C. Possibly, the unknown peaks are desorption of HCHO from depolymerization of tri/poly-oxymethylene, because of easy oligomerization of gaseous HCHO during pre-adsorption of HCHO [44]. The behavior of HCHO desorption from 5% Pt/Mn-TiO_2 at dry condition is similar. But the introduced water makes a great difference between 5% Pt/Mn-TiO_2 and Mn-TiO_2. The temperatures for HCHO emission are obviously reduced, implying promotion effect of moisture on desorption of HCHO. It is ascribed to inhibition of oligomerization in presence of water vapor [44]. In fact, HCHO at oligomerization state is oxidized by overcoming extra barrier energy, which gives an explanation for less CO_2 yield in the absence of moisture.

3.3. Reaction mechanism

For a deep insight of mechanism for low-temperature oxidation of HCHO over single-atom Pt catalyst, in-situ DRIFTS is performed. Under exposure of polluted stream containing gaseous HCHO, appearance of several peaks occurs to the spectra of after-treated 0.5% Pt/Mn-TiO2 as depicted in Fig. 1112(a). The peaks (γ(CH) = 2747 cm^{-1}, ν(C−O) = 1099 cm^{-1}) belonging to dioxymethylene (H2CO2, DOM) and the peaks (ν(CH) = 2957 cm^{-1}, νas(−COO) = 1576 cm^{-1}, δ(CH) = 1363 cm^{-1}, νs(−COO) = 1312 cm^{-1}) attributing to formate species (HCOOH/HCOO—) and the peaks (ν(CH) = 2863 cm^{-1}, ν(> C═O) = 1658 cm^{-1}) for HCHO are observed immediately within 1 min [24,45]. Simultaneously, the peaks maximized at between 3580 cm^{-1} and 3388 cm^{-1} of H_2O and the peak at 3250 cm^{-1} of −OH group appear. With time, the intensities of these peaks increase, as a sign of accumulation of substrate on catalyst and increasing formation of intermediates (H_2CO_2, HCOOH/$HCOO^-$) and products (H_2O, CO_2). Sequentially, the introduction of feed gas containing 20% O_2 leads to the changes gradually. As shown in Fig. 12(b), the intensities of characteristic peaks for H_2O and CO_2 increase within 1 min initially and then decrease in due time. With the time-dependent variation of products, the peaks of intermediate H_2CO_2 become weak, but the peaks for HCOOH/$HCOO^-$ become more obvious. An abnormal phenomenon happens to substrate HCHO. The relative intensity of the peak at 2863 cm^{-1} for C−H vibration of HCHO declines slightly with retention time, which means a little amount of HCHO is oxidized by dry air. However, the peak of > C═O group for HCHO at 1658 cm^{-1} is weakened and even becomes negative, implying consumption of adsorbed HCHO. Actually, the easy occurrence of aldol condensation at dry condition leads to oligomerization of HCHO by consuming > C═O groups, which not only gives an explanation for the unusual change in DRIFTS but also is in agreement with HCHO-TPD.

In fact, much effort has been paid on study of reaction mechanism for HCHO oxidation by taking theoretical analysis of TiO_2-based model catalysts [38–40]. By associating our observations with other reports, the pathway for catalytic oxidation of HCHO over Pt-based catalyst is

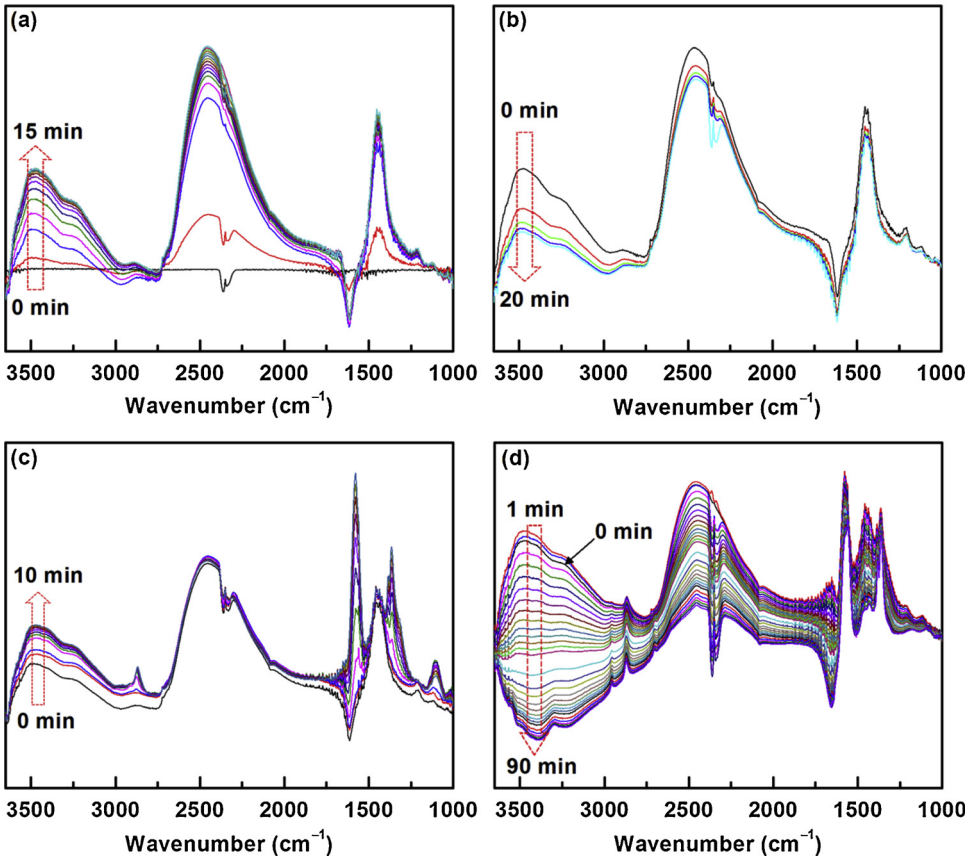

Fig. 13. Combination of isotope tracer and *in-situ* DRIFTS of HCHO of 0.5% Pt/Mn-TiO_2, (a) the first-time pre-adsorption of D_2O, (b) evacuation after H-D exchange, (c) adsorption of HCHO, (d) 20% O_2/He flowing through sample at room temperature.

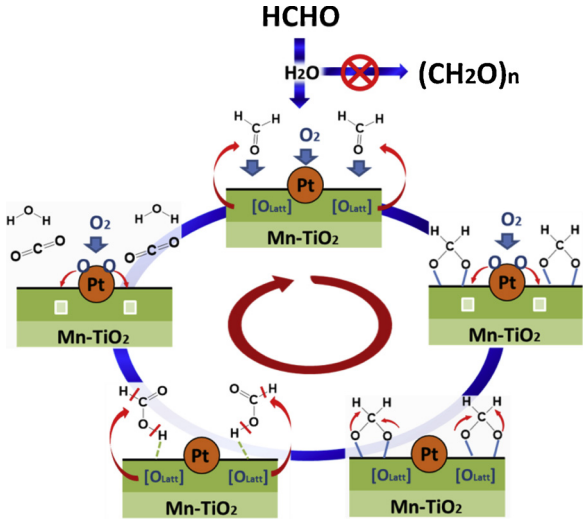

Scheme 1. Illustration of reaction mechanism about catalytic oxidation of HCHO over Pt/Mn-TiO_2.

proposed as follows: HCHO → CH_2O_2 → HCOOH/$HCOO^-$ → CO_2 + H_2O [45,46]. At the first stage, the participation of water vapor inhibits condensation of HCHO into $(HCHO)_n$ (n ≥ 3), and facilitates preliminary oxidation into CH_2O_2 [45]. Because of instability of CH_2O_2, it tends to isomerize into HCOOH and then dissociate into $HCOO^-$ anion. Finally, HCOOH/$HCOO^-$ is completely decomposed into H_2O and CO_2 over the catalyst. According to literatures, the surficial −OH group coming from adsorbed/generated water is advantageous to catalytic oxidation, so the deep oxidation of carbonic species is inhibited by loss of −OH group in dry gas stream [22,24,47].

For more information about humidity influence, hydrogen upon catalyst is exchanged to deuterium by using deuteroxide (D_2O) to avoid interference of H_2O derived from oxidation. As exhibited in Fig. 13(a–b), the appearance of the peaks maximized at 2470 cm^{-1}, 1438 cm^{-1} and 2290 cm^{-1} indicates success in H−D exchange. The peaks of H_2O/−OH are weakened by deuteration, and even the peak for bending vibration of −OH at 1613 cm^{-1} becomes negative. After introduction of HCHO, the peaks of H_2O increase with retention time but there is no obvious change to D_2O in Fig. 13(c), indicating accumulation of H_2O and no loss of D_2O during oxidation of HCHO. Because of limited quantity of oxygen adsorbed on catalyst, HCHO is partially oxidized into several intermediates like CH_2O_2 and HCOOH/$HCOO^-$, which is the same to the previous results of HCHO-DRIFTS. If H-D exchange takes place to C−H bond, a peak must appear at around 2100 cm^{-1} assigned to stretching vibration of C−D bond. However, this peak cannot be observed. When the stream is switched to 20% O_2/He, the changes of characteristic peaks with retention time in Fig. 13(d) are similar to observations of HCHO-DRIFTS without H−D exchange. Namely, the further decomposition of intermediates (H_2CO_2/HCOOH) by dry 20% O_2/He is inhibited with gradual loss of D_2O/—OD and H_2O/—OH, which is in accordance with published works [22,30,48]. Therefore, it is concluded that the role of moisture is mainly reflected in aspects involving the inhibition of side-reactions and facilitation of deep oxidation.

With comprehension of the *in-situ* DRIFTS, it is proposed that oxidation of HCHO obeys Mars-van-Krevelen mechanism [10,49–52]. The multiple steps are illustrated by Scheme 1. Firstly, HCHO is oxidized into CH_2O_2 by O_{Latt} species interconnected with Pt atom, resulting in formation of oxygen vacancy on the support which is denoted as [Pt-□-S]. Simultaneously, self-oligomerization of HCHO is prevented by

introduction of water vapor decreasing energy barrier for activation of HCHO. CH_2O_2 is fast converted into HCOOH and sequentially is oxidized into H_2O and CO_2 over catalyst. Finally, oxygen vacancy is refilled by activating molecular oxygen. As recently reported by Yang's group, the chemical adsorption of HCHO on surficial vacancy oxygen of TiO_2 is clearly watched by high-resolution AFM, which clarifies it feasible to adsorb-active-oxidize HCHO by O_{Latt} species on the surface of TiO_2 in the proposed mechanism [53]. During catalytic process, the participation of water can assist transformation of the intermediates, because additive water and surficial hydroxyl group derived from water can activate intermediates and facilitate desorption of products such as CO_2, which reduces energy barrier and drives reaction to positively proceed [25,48]. Notably, the recyclable consumption-supplementation of O_{Latt} determines the progress of the reaction. With similarity to Mars-van-Krevelen mechanism of CO oxidation over TiO_2-supported Au [49], O_{Latt} coordinated on Pt can be consumed to oxidize HCHO as well as intermediates and results in unsaturated coordination of Pt that plays a role to further activate molecular oxygen and provide active O_{Latt} for reaction, thereby ensuing an enclosed oxygen circulation. Since the SMSI effect facilitates activation and mobility of O_{Latt}, single-atom Pt catalysts prepared by redox-driven hydrolysis precipitation exhibit remarkable performance in low-temperature oxidation of HCHO.

4. Conclusions

In summary, we have successfully anchored single-atom Pt on surface of Mn-TiO_2 support by redox-driven hydrolysis precipitation as confirmed by multiple characterizations such as Cs-HAADF-STEM and XAFS. Because of enhancement of interaction between Pt atom and support, the redox properties of catalyst are improved, especially, the reactivity of lattice oxygen in surficial layer within support is promoted, so the as-prepared material exhibits a remarkable performance in low-temperature oxidation of HCHO in flowing gas. 0.5% Pt/Mn-TiO_2 (actual Pt content = 0.47%) is screened out as an optimal catalyst with outstanding activity as well as acceptable cost. Under catalysis of 0.5% Pt/Mn-TiO_2, high-concentration (100 ppm) HCHO is completely removed at room temperature with conditions of WHSV = 60,000 mL/(g h) and RH = 50%. Even when WHSV increases to 120,000 mL/(g h), more than 60% CO_2 yield is achieved from oxidation of high-concentration HCHO in the case of RH = 50%. Higher relative humidity is beneficial for oxidation of HCHO, so CO_2 yield increases to above 90% with conditions of RH = 80% and WHSV = 120,000 mL/(g h). Also, 0.5% Pt/Mn-TiO_2 is effective to clean indoor low-concentration HCHO and the outstanding performance can be remained for a long time at simulated condition. By correlation of structure and performance, it is revealed that HCHO oxidation over Pt catalyst obeys Mars-van-Krevelen mechanism where lattice oxygen on surface plays an important role, and during reaction water vapor has influence mainly on inhabitation of side reactions as well as facilitation of deep oxidation.

Declaration of Competing Interest

The authors declare that they have no known competing financial interests or personal relationships that could have appeared to influence the work reported in this paper.

Acknowledgements

This work was supported by National Nature Science Foundation of China [No. 21806162]; the FJIRSM&IUE Joint Research Fund [No. RHZX-2018-002]; the "Cooperation of Industry-University-Institute and Scientific and Technological Cooperation" of Xiamen [3502Z20182006]; the "Key Research Program of Frontier Sciences" from Chinese Academy of Sciences [No. QYZDB-SSW-DQC022].

Appendix A. Supplementary data

Supplementary material related to this article can be found, in the online version, at doi:https://doi.org/10.1016/j.apcatb.2019.118013.

References

[1] Y.J. Chen, S.F. Ji, C. Chen, Q. Peng, D.S. Wang, Y.D. Li, Single-atom catalysts: synthetic strategies and electrochemical applications, Joule 2 (2018) 1242–1264, https://doi.org/10.1016/j.joule.2018.06.019.
[2] H. Yan, X.X. Zhao, N. Guo, Z.Y. Lyu, Y.H. Du, S.B. Xi, R. Guo, C. Chen, Z.X. Chen, W. Liu, C.H. Yao, J. Li, S.J. Pennycook, W. Chen, C.L. Su, C. Zhang, J. Lu, Atomic engineering of high-density isolated Co atoms on graphene with proximal-atom controlled reaction selectivity, Nat. Commun. 9 (2018) 3197, https://doi.org/10.1038/s41467-018-05754-9.
[3] J. Jones, H.F. Xiong, A.T. DeLaRiva, E.J. Peterson, H. Pham, S.R. Challa, G. Qi, S. Oh, M.H. Wiebenga, X.I. Pereira Hernández, Y. Wang, A.K. Datye, Thermally stable single-atom platinum-on-ceria catalysts *via* atom trapping, Science 353 (2016) 150–154 http://science.sciencemag.org/content/sci/353/6295/150.full.pdf.
[4] Z.Y. Li, Z. Yuan, X.N. Li, Y.X. Zhao, S.G. He, CO oxidation catalyzed by single gold atoms supported on aluminum oxide clusters, J. Am. Chem. Soc. 136 (2014) 14307–14313, https://doi.org/10.1021/ja508547z.
[5] J. Lin, A.Q. Wang, B.T. Qiao, X.Y. Liu, X.F. Yang, X.D. Wang, J.X. Liang, J. Li, J.Y. Liu, T. Zhang, Remarkable performance of Ir_1/FeO_x single-atom catalyst in water gas shift reaction, J. Am. Chem. Soc. 135 (2013) 15314–15317, https://doi.org/10.1021/ja408574m.
[6] B.T. Qiao, A.Q. Wang, X.F. Yang, L.F. Allard, Z. Jiang, Y.T. Cui, J.Y. Liu, J. Li, T. Zhang, Single-atom catalysis of CO oxidation using Pt_1/FeO_x, Nat. Chem. 3 (2011) 634–641, https://doi.org/10.1038/nchem.1095.
[7] X.F. Yang, A.Q. Wang, B.T. Qiao, J. Li, J.Y. Liu, T. Zhang, Single-atom catalysts: a new frontier in heterogeneous catalysis, Acc. Chem. Res. 46 (2013) 1740–1748, https://doi.org/10.1021/ar300361m.
[8] H.L. Li, L.B. Wang, Y.Z. Dai, Z.T. Pu, Z.H. Lao, Y.W. Chen, M.L. Wang, X.S. Zheng, J.F. Zhu, W.H. Zhang, R. Si, C. Ma, J. Zeng, Synergetic interaction between neighbouring platinum monomers in CO_2 hydrogenation, Nat. Nanotechnol. 13 (2018) 411–417, https://doi.org/10.1038/s41565-018-0089-z.
[9] P.Z. Chen, T.P. Zhou, L.L. Xing, K. Xu, Y. Tong, H. Xie, L.D. Zhang, W.S. Yan, W.S. Chu, C.Z. Wu, Y. Xie, Atomically dispersed iron–nitrogen species as electrocatalysts for bifunctional oxygen evolution and reduction reactions, Angew. Chem. Int. Ed. 56 (2017) 610–614, https://doi.org/10.1002/anie.201610119.
[10] J. Chen, D.X. Yan, Z. Xu, X. Chen, X. Chen, W.J. Xu, H.P. Jia, J. Chen, A novel redox precipitation to synthesize Au-Doped α-MnO_2 with high dispersion toward low-temperature oxidation of formaldehyde, Environ. Sci. Technol. 52 (2018) 4728–4737, https://doi.org/10.1021/acs.est.7b06039.
[11] J. Chen, X. Chen, D.X. Yan, M.Z. Jiang, W.J. Xu, H. Yu, H.P. Jia, A facile strategy of enhancing interaction between cerium and manganese oxides for catalytic removal of gaseous organic contaminants, Appl. Catal. B - Environ. 250 (2019) 396–407, https://doi.org/10.1016/j.apcatb.2019.03.042.
[12] J.A. Dean, Lange's Handbook of Chemistry, 16th ed., McGraw-Hill, New York, 1992.
[13] P. Liu, G.L. Wei, H.P. He, X.L. Liang, H.L. Chen, Y.F. Xi, J.X. Zhu, The catalytic oxidation of formaldehyde over palygorskite-supported copper and manganese oxides: catalytic deactivation and regeneration, Appl. Surf. Sci. 464 (2019) 287–293, https://doi.org/10.1016/j.apsusc.2018.09.070.
[14] Z.Y. Fan, W.J. Fang, Z.X. Zhang, M.X. Chen, W.F. Shangguan, Highly active rod-like Co_3O_4 catalyst for the formaldehyde oxidation reaction, Catal. Commun. 103 (2018) 10–14, https://doi.org/10.1016/j.catcom.2017.09.003.
[15] J. Zhang, Y. Jin, C.Y. Li, Y.N. Shen, L. Han, Z.X. Hu, X.W. Di, Z.L. Liu, Creation of three-dimensionally ordered macroporous Au/CeO_2 catalysts with controlled pore sizes and their enhanced catalytic performance for formaldehyde oxidation, Appl. Catal. B - Environ. 91 (2009) 11–20, https://doi.org/10.1016/j.apcatb.2009.05.001.
[16] J.F. Qu, D.Y. Chen, N.J. Li, Q.F. Xu, H. Li, J.H. He, J.M. Lu, 3D gold-modified cerium and cobalt oxide catalyst on a graphene aerogel for highly efficient catalytic formaldehyde oxidation, Small 15 (2019) 1804415, , https://doi.org/10.1002/smll.201804415.
[17] X.Y. Chen, M. Chen, G.Z. He, F. Wang, G.Y. Xu, Y.B. Li, C.B. Zhang, H. He, Specific role of potassium in promoting Ag/Al_2O_3 for catalytic oxidation of formaldehyde at low temperature, J. Phys. Chem. C 122 (2018) 27331–27339, https://doi.org/10.1021/acs.jpcc.8b07160.
[18] L. Ma, D.S. Wang, J.H. Li, B.Y. Bai, L.X. Fu, Y.D. Li, Ag/CeO_2 nanospheres: efficient catalysts for formaldehyde oxidation, Appl. Catal. B - Environ. 148–149 (2014) 36–43 http://www.sciencedirect.com/science/article/pii/S0926337313006644.
[19] X.C. Sun, J. Lin, H.L. Guan, L. Li, L. Sun, Y.H. Wang, S. Miao, Y. Su, X.D. Wang, Complete oxidation of formaldehyde over TiO_2 supported subnanometer Rh catalyst at ambient temperature, Appl. Catal. B - Environ. 226 (2018) 575–584, https://doi.org/10.1016/j.apcatb.2018.01.011.
[20] Y.B. Li, X.Y. Chen, C.Y. Wang, C.B. Zhang, H. He, Sodium enhances Ir/TiO_2 activity for catalytic oxidation of formaldehyde at ambient temperature, ACS Catal. 8 (2018) 11377–11385, https://doi.org/10.1021/acscatal.8b03026.
[21] Y.B. Li, C.B. Zhang, H. He, J.H. Zhang, M. Chen, Influence of alkali metals on Pd/TiO_2 catalysts for catalytic oxidation of formaldehyde at room temperature, Catal. Sci. Tech. 6 (2016) 2289–2295, https://doi.org/10.1039/C5CY01521A.

[22] Y.B. Li, C.B. Zhang, J.Z. Ma, M. Chen, H. Deng, H. He, High temperature reduction dramatically promotes Pd/TiO_2 catalyst for ambient formaldehyde oxidation, Appl. Catal. B - Environ. 217 (2017) 560–569, https://doi.org/10.1016/j.apcatb.2017.06.023.
[23] C.B. Zhang, Y.B. Li, Y.F. Wang, H. He, Sodium-promoted Pd/TiO_2 for catalytic oxidation of formaldehyde at ambient temperature, Environ. Sci. Technol. 48 (2014) 5816–5822, https://doi.org/10.1021/es4056627.
[24] C.B. Zhang, F.D. Liu, Y.P. Zhai, H. Ariga, N. Yi, Y.C. Liu, K. Asakura, M. Flytzani Stephanopoulos, H. He, Alkali-metal-promoted Pt/TiO_2 opens a more efficient pathway to formaldehyde oxidation at ambient temperatures, Angew. Chem. Int. Ed. 51 (2012) 9628–9632, https://doi.org/10.1002/anie.201202034.
[25] D.W. Kwon, P.W. Seo, G.J. Kim, S.C. Hong, Characteristics of the HCHO oxidation reaction over Pt/TiO_2 catalysts at room temperature: the effect of relative humidity on catalytic activity, Appl. Catal. B - Environ. 163 (2015) 436–443, https://doi.org/10.1016/j.apcatb.2014.08.024.
[26] L. Wang, H.Q. Yue, Z.L. Hua, H.Y. Wang, X.B. Li, L.C. Li, Highly active Pt/Na_xTiO_2 catalyst for low temperature formaldehyde decomposition, Appl. Catal. B - Environ. 219 (2017) 301–313, https://doi.org/10.1016/j.apcatb.2017.07.073.
[27] M. Randy, R. Marion, D.P. Sullivan, M.G. Apte, Formaldehyde and other volatile organic chemical emissions in four FEMA temporary housing units, Environ. Sci. Technol. 43 (2009) 5626–5632, https://doi.org/10.1021/es9011178.
[28] C.H. Ao, S.C. Lee, Enhancement effect of TiO_2 immobilized on activated carbon filter for the photodegradation of pollutants at typical indoor air level, Appl. Catal. B - Environ. 44 (2003) 191–205, https://doi.org/10.1016/S0926-3373(03)00054-7.
[29] M.B. Chang, C.C. Lee, Destruction of formaldehyde with dielectric barrier discharge plasmas, Environ. Sci. Technol. 29 (1995) 181–186, https://doi.org/10.1021/es00001a023.
[30] C.B. Zhang, H. He, A comparative study of TiO_2 supported noble metal catalysts for the oxidation of formaldehyde at room temperature, Catal. Today 126 (2007) 345–350, https://doi.org/10.1016/j.cattod.2007.06.010.
[31] L.H. Nie, J.G. Yu, X.Y. Li, B. Cheng, G. Liu, M. Jaroniec, Enhanced performance of NaOH-modified Pt/TiO_2 toward room temperature selective oxidation of formaldehyde, Environ. Sci. Technol. 47 (2013) 2777–2783, https://doi.org/10.1021/es3045949.
[32] B. de Rivas, R. López Fonseca, C. Jiménez González, J.I. Gutiérrez Ortiz, Synthesis, characterisation and catalytic performance of nanocrystalline Co_3O_4 for gas-phase chlorinated VOC abatement, J. Catal. 281 (2011) 88–97, https://doi.org/10.1016/j.jcat.2011.04.005.
[33] B. Ravel, M. Newville, ATHENA, ARTEMIS, HEPHAESTUS: data analysis for X-ray absorption spectroscopy using IFEFFIT, J. Synchrotron Radiat. 12 (2005) 537–541, https://doi.org/10.1107/S0909049505012719.
[34] L. Nie, D.H. Mei, H.F. Xiong, B. Peng, Z.B. Ren, X.I.P. Hernandez, A. DeLaRiva, M. Wang, M.H. Engelhard, L. Kovarik, A.K. Datye, Y. Wang, Activation of surface lattice oxygen in single-atom Pt/CeO_2 for low-temperature CO oxidation, Science 358 (2017) 1419–1423 http://science.sciencemag.org/content/sci/358/6369/1419.full.pdf.
[35] L.D. Li, Q. Shen, J. Cheng, Z.Q. Hao, Catalytic oxidation of NO over TiO_2 supported platinum clusters I. Preparation, characterization and catalytic properties, Appl. Catal. B - Environ. 93 (2010) 259–266, https://doi.org/10.1016/j.apcatb.2009.09.037.
[36] S.-H. Chien, B.N. Shelimov, D.E. Resasco, E.H. Lee, G.L. Haller, Characterization of the interaction between rhodium and titanium oxide by XPS, J. Catal. 77 (1982) 301–303, https://doi.org/10.1016/0021-9517(82)90172-5.
[37] J. Chen, X. Chen, X. Chen, W.J. Xu, Z. Xu, H.P. Jia, J. Chen, Homogeneous introduction of CeO_y into MnO_x-based catalyst for oxidation of aromatic VOCs, Appl. Catal. B - Environ. 224 (2018) 825–835, https://doi.org/10.1016/j.apcatb.2017.11.036.
[38] S.R. Li, X.Q. Lu, W.Y. Guo, H.Y. Zhu, M. Li, L.M. Zhao, Y. Li, H.H. Shan, Formaldehyde oxidation on the Pt/TiO_2(101) surface: a DFT investigation, J. Organomet. Chem. 704 (2012) 38–48, https://doi.org/10.1016/j.jorganchem.2012.01.002.
[39] X.Y. Wang, Z.B. Rui, Y.Q. Zeng, H.B. Ji, Z. Du, Q.L. Rao, Synergetic effect of oxygen vacancy and Pd site on the interaction between Pd/Anatase TiO_2(101) and formaldehyde: a density functional theory study, Catal. Today 297 (2017) 151–158, https://doi.org/10.1016/j.cattod.2017.06.037.
[40] G.F. Wu, C.H. Zhao, X. Zhou, J.H. Chen, Y.Q. Li, Y. Chen, The interaction between HCHO and TiO_2 (1 0 1) surface without and with water and oxygen molecules, Appl. Surf. Sci. 455 (2018) 410–417, https://doi.org/10.1016/j.apsusc.2018.05.206.
[41] C.J. Jia, M. Schwickardi, C. Weidenthaler, W. Schmidt, S. Korhonen, B.M. Weckhuysen, F. Schüth, Co_3O_4–SiO_2 nanocomposite: a very active catalyst for CO oxidation with unusual catalytic behavior, J. Am. Chem. Soc. 133 (2011) 11279–11288, https://doi.org/10.1021/ja2028926.
[42] C.J. Jia, Y. Liu, H. Bongard, F. Schüth, Very low temperature CO oxidation over colloidally deposited gold nanoparticles on $Mg(OH)_2$ and MgO, J. Am. Chem. Soc. 132 (2010) 1520–1522, https://doi.org/10.1021/ja909351e.
[43] State Bureau of Quality and Technical Supervision, Ministry of Environmental Protection of the People's Republic of China, M.o.H.o.t.P.s.R.o. China (Eds.), Indoor Air Quality Standard, China Standard Press, Beijing, 2002, http://www.mee.gov.cn/image20010518/5295.pdf.
[44] F.X.L. i. Xamena, C.O. Areán, S. Spera, E. Merlo, A. Zecchina, Formaldehyde oligomerization on silicalite: an FTIR and NMR study, Catal. Lett. 95 (2004) 51–55, https://doi.org/10.1023/B:CATL.0000023721.90964.e2.
[45] Z.X. Yan, Z.H. Xu, J.G. Yu, M. Jaroniec, Highly active mesoporous ferrihydrite supported Pt catalyst for formaldehyde removal at room temperature, Environ. Sci. Technol. 49 (2015) 6637–6644, https://doi.org/10.1021/acs.est.5b00532.
[46] L.H. Nie, Y.Q. Zheng, J.G. Yu, Efficient decomposition of formaldehyde at room temperature over Pt/honeycomb ceramics with ultra-low Pt content, Dalton Trans. 43 (2014) 12935–12942, https://doi.org/10.1039/C4DT01323A.
[47] A. Yusuf, C. Snape, J. He, H.H. Xu, C.J. Liu, M. Zhao, G.Z. Chen, B.C. Tang, C.J. Wang, J.W. Wang, S.N. Behera, Advances on transition metal oxides catalysts for formaldehyde oxidation: a review, Catal. Rev. 59 (2017) 189–233, https://doi.org/10.1080/01614940.2017.1342476.
[48] J.L. Wang, P.Y. Zhang, J.G. Li, C.J. Jiang, R. Yunus, J. Kim, Room-temperature oxidation of formaldehyde by layered manganese oxide: effect of water, Environ. Sci. Technol. 49 (2015) 12372–12379, https://doi.org/10.1021/acs.est.5b02085.
[49] D. Widmann, R.J. Behm, Dynamic surface composition in a Mars-van Krevelen type reaction: CO oxidation on Au/TiO_2, J. Catal. 357 (2018) 263–273, https://doi.org/10.1016/j.jcat.2017.11.005.
[50] S.J. Park, I. Bae, I.-S. Nam, B.K. Cho, S.M. Jung, J.-H. Lee, Oxidation of formaldehyde over Pd/Beta catalyst, Chem. Eng. J. 195–196 (2012) 392–402, https://doi.org/10.1016/j.cej.2012.04.028.
[51] K.T. Chuang, B. Zhou, S.M. Tong, Kinetics and mechanism of catalytic oxidation of formaldehyde over hydrophobic catalysts, Ind. Eng. Chem. Res. 33 (1994) 1680–1686, https://doi.org/10.1021/ie00031a007.
[52] C.Y. Li, Y.N. Shen, M.L. Jia, S.S. Sheng, M.O. Adebajo, H.Y. Zhu, Catalytic combustion of formaldehyde on gold/iron-oxide catalysts, Catal. Commun. 9 (2008) 355–361, https://doi.org/10.1016/j.catcom.2007.06.020.
[53] H.C. Wang, X.Y. Zhao, C.Q. Huang, X.C. Jin, D. Wei, D.X. Dai, Z.B. Ma, W.X. Li, X.M. Yang, Adsorption features of formaldehyde on TiO_2(110) surface probed by high-resolution scanning tunnelling microscopy, J. Phys. Chem. Lett. 10 (2019) 3352–3358, https://doi.org/10.1021/acs.jpclett.9b00522.